nature communications

Article

https://doi.org/10.1038/s41467-023-41996-y

PdCu nanoalloy decorated photocatalysts for efficient and selective oxidative coupling of methane in flow reactors

Received: 18 June 2022

Accepted: 26 September 2023

Published online: 10 October 2023

Check for updates

Xiyi Li[1], Chao Wang[1], Jianlong Yang[2], Youxun Xu[1], Yi Yang[3], Jiaguo Yu[4], Juan J. Delgado[5,6], Natalia Martsinovich[7], Xiao Sun[8], Xu-Sheng Zheng[9], Weixin Huang[8] & Junwang Tang[1,10]

Methane activation by photocatalysis is one of the promising sustainable technologies for chemical synthesis. However, the current efficiency and stability of the process are moderate. Herein, a PdCu nanoalloy (~2.3 nm) was decorated on TiO_2, which works for the efficient, stable, and selective photocatalytic oxidative coupling of methane at room temperature. A high methane conversion rate of 2480 μmol g^{-1} h^{-1} to C_2 with an apparent quantum efficiency of ~8.4% has been achieved. More importantly, the photocatalyst exhibits the turnover frequency and turnover number of 116 h^{-1} and 12,642 with respect to PdCu, representing a record among all the photocatalytic processes (λ > 300 nm) operated at room temperature, together with a long stability of over 112 hours. The nanoalloy works as a hole acceptor, in which Pd softens and weakens C-H bond in methane and Cu decreases the adsorption energy of C_2 products, leading to the high efficiency and long-time stability.

The discovery of fire ice, together with the shale gas has indicated that methane reserve on the earth is much more than the sum of coal and oil, which renders methane as one of the most promising future energy sources and chemical feedstocks[1,2]. However, due to the inert nature of methane (high symmetrical structure, low polarisability, high ionization potential, and highly stable C-H bond), the activation energy for methane conversion is high, resulting in harsh reaction conditions, such as high temperatures, strong oxidants, or strong acidic environments[3–5]. Therefore, the direct conversion of methane via traditional processes has suffered from several barriers to commercialisation, including the deactivation of catalysts (e.g., coke accumulation and sintering), low selectivity of desired products (e.g., overoxidation), large CO_2 emission and high capital costs[6–8]. Furthermore, this does not align with the goals of transition to clean technology with net zero carbon emissions as underscored by the UN Climate Change Conference UK 2021 (COP 26).

Photocatalysis, a developing green technology, utilises photon-induced charge carriers (electrons/holes) to pre-activate stable chemical bonds (e.g., O-H, C = O, and C-H), thus lowering activation barriers and driving thermodynamically unfavourable chemical reactions (water splitting, CO_2 reduction and methane conversion, etc.) under mild conditions[7,9,10]. Among various methane conversion reactions,

[1]Department of Chemical Engineering, University College London, London WC1E 7JE, UK. [2]Key Lab of Synthetic and Natural Functional Molecule Chemistry of Ministry of Education, the Energy and Catalysis Hub, College of Chemistry and Materials Science, Northwest University, Xi'an, P. R. China. [3]State Key Laboratory of Advanced Technology for Materials Synthesis and Processing, Wuhan University of Technology, Wuhan 430070, China. [4]Laboratory of Solar Fuel, Faculty of Materials Science and Chemistry, China University of Geosciences, 388 Lumo Road, Wuhan 430074, China. [5]Departamento de Ciencia de los Materiales e Ingeniería Metalúrgica y Química Inorgánica, Facultad de Ciencias, Universidad de Cádiz, Campus Rio San Pedro, 11510 Puerto Real, Cádiz, Spain. [6]IMEYMAT, Instituto de Microscopía Electrónica y Materiales, Puerto Real 11510, Spain. [7]Department of Chemistry, University of Sheffield, Sheffield S3 7HF, UK. [8]Hefei National Research Center for Physical Sciences at the Microscale, iChEM, Key Laboratory of Surface and Interface Chemistry and Energy Catalysis of Anhui Higher Education Institutes, School of Chemistry and Materials Science, University of Science and Technology of China, 230026 Hefei, China. [9]National Synchrotron Radiation Laboratory, University of Science and Technology of China, Hefei 230029 Anhui, China. [10]Industrial Catalysis Center, Department of Chemical Engineering, Tsinghua University, Beijing 100084, China. e-mail: junwang.tang@ucl.ac.uk

coupling of two methane molecules to produce C_2 products (C_2H_6/C_2H_4) is one of the most general and highly profitable processes[3,11], while it is much more challenging than C_1 production. We have recently reported the first example of photocatalytic oxidative coupling of methane (OCM) over CuO_x-Pt/TiO_2 in a flow reactor[12], which proved the concept while the C_2 yield rate was moderate (6.8 μmol h^{-1}) and the stability test only ran for 8 h.

Photocatalytic processes often exhibit high selectivity, however, the reported conversion rate and more importantly the stability are rather moderate, which are two equally important indexes, especially for future application[2]. Two important factors, Turnover frequency (TOF) and Turnover number (TON), reflecting both catalytic activity and stability, are robust to assess the photocatalysts. The majority of the reported photocatalytic methane coupling flow systems represent a rather moderate TOF < 5 h^{-1} or TON of <10. Very recently a few benchmark studies such as oxidative coupling with water over Pd/Ga_2O_3[13], non-oxidative coupling over Au/TiO_2[14], and oxidative coupling with oxygen over Au-ZnO/TiO_2[15], improved TON to a few hundred, with the assistance of deep UV light (254 nm)[13] or the thermal effect (140 °C)[15]. It is still a great challenge to achieve an efficient photocatalyst with both high TOF and TON for photocatalytic coupling of methane under ambient conditions.

A novel design strategy of multi-functional photocatalysts is necessary to achieve this goal, which requires the synergy of different components. Formation of bimetallic nanoalloy catalysts via combining one metal with another is one of the most effective and universal strategies. Successful examples have been reported in traditional methane conversion to obtain both high catalytic performance and resistance to deactivation, such as steam reforming of methane over AuNi[16] and dry reforming of methane over Ni-Cu/Mg(Al)O[17]. In photocatalytic methane conversion, three factors need to be considered to meet this versatile requirement, such as (i) high availability of photon-induced charge carriers; (ii) efficient and selective activation of the first C-H bond in CH_4; (iii) prolonged stability against coking and bleaching of active species.

Herein, a screening process was carried out assess a series of noble metals on the TiO_2 photocatalyst, which usually act as charge sinks to promote charge transfer in photocatalysis[18] and show unique catalytic performance for the C-H bond activation in thermocatalysis[19]. Pd shows exceptional activity as the most efficient co-catalyst but suffers from coke accumulation like a recent example in photocatalytic methane conversion over Pd/Ga_2O_3[20]. In traditional methane conversion, the coke resilience could be enhanced by the formation of nanoalloy with another active transition metal, e.g., PtCu, NiCu[21,22]. Thus, a series of non-noble transition metals as the second component were introduced to form bimetallic nanoalloys with Pd to enhance the stability. The incorporation of Cu is found to enhance both activity and resistance to coking of the photocatalyst. The PdCu nanoalloy decorated TiO_2 exhibits the highest methane conversion rate of 2480 μmol g^{-1} h^{-1} to C_2 products with the high quantum efficiency (AQE) of ~8.4% at 365 nm. Furthermore, PdCu/TiO_2 presents a TOF_{PdCu} of 116 h^{-1} and TON_{PdCu} of 12,642 for the conversion to C_2 products, which is 20 times higher than the recent benchmark results[14,23].

Results

Photocatalytic activity

Since noble metals are often regarded as charge sinks to promote charge separation to facilitate photocatalytic activity[18], photocatalytic OCM reactions were first investigated over different noble metals nanoparticles decorated TiO_2 (anatase) in a flow reactor using a 365 nm LED under room temperature and atmospheric pressure (Fig. 1a). Different effects on the C_2 yield rates were observed, following the trend: Pd/TiO_2 > Au/TiO_2 > Ag/TiO_2 > TiO_2 > Ru/TiO_2 > Pt/TiO_2. Compared with the low yield rate (ca. 4 μmol h^{-1}) of pristine TiO_2, an improvement of nearly 8 times is achieved after the loading of Pd. In addition to the enhancement of charge carrier transfer, such a promotion effect can also be attributed to the strong interaction between Pd nanoparticles and the C-H bond in CH_4[24,25]. Pd was then selected as the best co-catalyst and its loading amount was optimized (Supplementary Fig. 1). The C_2 yield rate exhibited a volcano trend with the increasing loading wt% of Pd. After reaching 32 μmol h^{-1} over $Pd_{0.1}$/TiO_2, less than 20% increase could be observed with a five-fold increase in Pd loading amount, and further increase of loading amount to 1 wt% resulted in decreased activity. This might be because excessive Pd nanoparticles obstruct the light penetration to TiO_2 by scattering and/or absorption[26,27]. Balancing the cost and performance of Pd cocatalyst, 0.1 wt% was selected as the optimum amount for the following study (denoted Pd/TiO_2 without specific notification). Unexpectedly, the performance of Pd/TiO_2 exhibited a declined trend when the reaction time was extended, as shown in Supplementary Fig. 2. In thermocatalytic methane conversion, the strong interaction of the catalyst with CH_4 (e.g., strong binding force to adsorbates or low activation energy barrier) often lead to consecutive reactions for coke accumulation[19,28]. A recent example in photocatalytic methane conversion over Pd/Ga_2O_3 also found the deposition of coke by a side reaction[20]. Thus, the deactivation of Pd/TiO_2 is likely due to the accumulation of cokes, which is proved later in this study.

Transition metals can be used to form alloys with another active metal to enhance the cokes resilience[21,22]. Thus, a group of transition metals were investigated to form nanoalloy with Pd and their molar amount was equal to that of Pd. Figure 1b shows that Cu and Ni both improve the Pd/TiO_2 activity for C_2 yield among Ni, Co, Cu, and Fe cocatalysts loaded photocatalysts, nearly 2.2 and 1.4 times higher than single Pd/TiO_2, respectively.

More interestingly, PdNi/TiO_2, PdCo/TiO_2, and PdFe/TiO_2, exhibit a declined trend similar to Pd/TiO_2 for C_2 yield rates, while the incorporation of Cu reverses the trend of C_2 yield rate (Supplementary Fig. 2), so the PdCu is the best.. The effect of the Pd: Cu ratio and the PdCu loading amount was also optimised as discussed alongside in Supplementary Fig. 3 and 4. The optimum sample is $Pd_{0.1}Cu_{0.1}$/TiO_2 and the real concentration of the cocatalyst was then analysed by ICP-OES to be Pd 0.089% and Cu 0.051% listed in Supplementary Table 1 (denoted PdCu/TiO_2 unless otherwise specified). Supplementary Fig. 5 further shows temporal C_2 yield on different photocatalysts. Both Cu/TiO_2 and PdCu/TiO_2 show an almost stable activity while Pd/TiO_2 activity keeps a fast decay and then a slow decay with time. The yield rate of C_2 on Pd/TiO_2 decreases by 50% when the reaction time is prolonged to 5 h. PdCu/TiO_2 represents the stable yield rate of ca. 57 μmol h^{-1} for 8 h. Supplementary Fig. 6 details the selectivity to C_2 products, CO_2, and C_3H_8. The introduction of Cu, Pd, and PdCu increases C_2 selectivity to 37%, 55%, and 57% compared with the pristine TiO_2 (13%), respectively, and the total methane conversion rate on PdCu/TiO_2 is more than 3 times higher than that of pristine TiO_2. Afterward, the ratio of CH_4 to O_2 was varied to investigate the optimum reaction conditions (Fig. 1c). When the ratio of CH_4 to O_2 is 53: 1, the C_2 yield rate reaches as high as 62 μmol h^{-1} (1240 μmol g^{-1} h^{-1}), corresponding to the methane conversion to C_2 rate of 124 μmol h^{-1} (2480 μmol g^{-1} h^{-1}), showing the leading position in the reported photocatalytic methane conversion to C_2 products processes under ambient conditions (Supplementary Table 2). The optimised catalyst also exhibits a high light utilisation efficiency with a apparent quantum efficiency (AQE) of ~8.4% at 365 nm. Excessive amounts of O_2 would generate more superoxide radicals $O_2^{\cdot-}$, which was considered as an active species to promote the conversion rate but also to increase overoxidation to CO_2[27,29]. Thus, as the O_2 amount is reduced (with the CH_4: O_2 ratio increased from 53: 1 to 373: 1), a slight decrease in methane conversion rate to ethane is observed. By contrast, the overoxidation to CO_2 shows a notable decrease to less than one third, from ca. 110 to 30 μmol h^{-1}, resulting in a high C_2 selectivity of ca. 75%. In addition, such high selectivity is comparable

https://doi.org/10.1038/s41467-023-41996-y

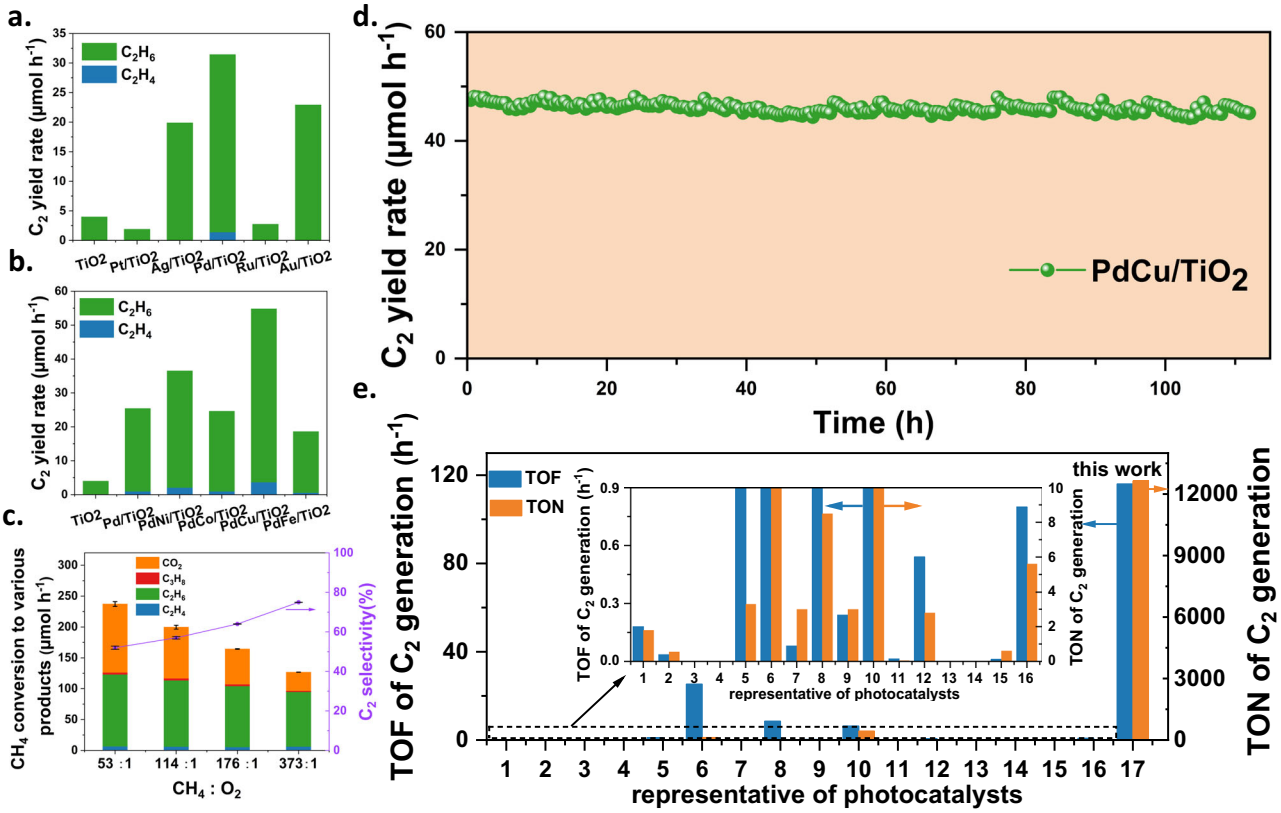

Fig. 1 | Photocatalytic OCM activity over PdCu nanoalloy decorated TiO_2. **a** C_2 yield rate over different noble co-catalysts decorated TiO_2 with the equal molar amount to Pd. **b** Influence of second transition metal cocatalysts with the equal molar amount to Pd on C_2 production at 1.5-hour run. **c** CH_4 total conversion rate and C_2 selectivity over PdCu/TiO_2 with different CH_4: O_2 ratios (the ratios were 53: 1, 114: 1, 176: 1, and 373: 1, respectively). Error bars (standard deviation) in the figure were obtained from three sampling runs. **d** C_2 synthesis over PdCu/TiO_2 during an intermittent 112-hour reaction with the CH_4: O_2 ratio of 373: 1, these data were collected every 30 min. **e** Summary of turnover frequency (TOF) and turnover number (TON) achieved on PdCu/TiO_2 and other reported representative photocatalysts (λ > 300 nm) at room temperature (1: AuPd/ZnO[79]; 2: Au/ZnO[80]; 3: Ga_2O_3-K[81]; 4: MgO-SiO_2[82]; 5: Ce-Al_2O_3[83]; 6: Au/WO_3[23]; 7: Ag-$H_3PW_{12}O_{40}$/TiO_2[33]; 8: Pt-CuO_x/TiO_2[12]; 9: Pt/Ga-TiO_2-SiO_2[84]; 10: Au/TiO_2[14]; 11: TiO_2/SiO_2[85]; 12: SiO_2-Al_2O_3-TiO_2[86]; 13: H-MOR[87]; 14: FSM-16[88]; 15: GaN: ZnO[89]; 16: $Zn_5(OH)_8Cl_2{\cdot}H_2O$[90], 17: this work.). The insert figure is the zoomed rectangle region indicated with the dash line in the main panel, showing the range of TON between 0–10 and TOF between 0–0.9. Among them, the values of photocatalyst 3, 4, 13 and 14 are still too small to see even in the enlarged insert. The calculation method is shown in the Method section. Reaction condition in (**a**, **b**): gas hourly space velocity (GHSV = 342,000 mL g_{cat}^{-1} $hour^{-1}$), CH_4: O_2 = 114: 1, 10% of CH_4, Ar as balance gas, 365 nm LED 40 W, 30 °C; the reaction condition in (**c**) was similar to the above except the ratio of CH_4: O_2 and the reaction condition in (**d**) was also similar except the ratio of CH_4: O_2 was changed to 373: 1. Source data are provided as a Source Data file.

to the most excellent OCM catalysts (e.g., Li/MgO; Mn/Na_2WO_4/SiO_2) by thermocatalysis operated at >873 K[30,31]. Therefore, the optimised experimental condition is the gas hourly space velocity (GHSV) of 342,000 mL g_{cat}^{-1} $hour^{-1}$ with the ratio of CH_4 to O_2 at 373: 1 operated at room temperature.

The control experiments were also carried out and they show that no products are observed in the absence of methane, without photocatalysts or under dark conditions, proving that this is a photocatalytic process and the only carbon source is methane (Supplementary Fig. 7). To further confirm methane as the only carbon source[13],CH_4 isotope experiment was carried out (Supplementary Fig. 8). Dominant peaks attributed to main products and their molecular fragments can be observed using $^{12}CH_4$ as the feedstock, such as C_2H_6 (m/z = 30, 29, 28, 27, 26), C_2H_4 (m/z = 28, 27, 26) and CO_2 (m/z = 44, 28), respectively. When the ^{13}C-labelled CH_4 is used as the feedstock, the m/z of dominant peaks increase by 2 for both $^{13}C_2H_6$ (32, 31, 30, 29, 28) and $^{13}C_2H_4$ (m/z = 30, 29, 28). In parallel, the m/z of $^{13}CO_2$ (m/z = 45, 29) also shifts by 1 compared with that observed under the $^{12}CH_4$ atmosphere. Although some m/z for product $^{13}C_2H_6$ may overlap with other components (e.g., m/z of 32 for $^{13}C_2H_6$ and O_2, m/z of 30 for $^{13}C_2H_4{\cdot}$ and $^{12}C_2H_6$), the intensity of these m/z is much higher than that using $^{12}CH_4$ as the feedstock. This result further indicates that the large contribution for the intensity at m/z 32 and m/z 30 should come from the ^{13}C isotope-labelling products. More importantly, the m/z of 31 indicating the formation of $^{13}C_2H_5{\cdot}$ can be observed under the $^{13}CH_4$ atmosphere. The disappearance of m/z = 26 and 27 for molecular fragments of $^{12}C_2H_2{\cdot}$ and $^{12}C_2H_3{\cdot}$ further confirms the carbon source from $^{13}CH_4$.

Then, a long-term stability test was carried out under the optimised condition as shown in Fig. 1d. The CH_4 conversion rate to C_2 remains almost stable during the whole term of the 112-hour test despite a slight change likely due to slight fluctuation of the gas flow rates. This result indicates the high stability of PdCu nanoalloy as the catalytic active site. This is one of the longest times (>100 h) for stability tests in photocatalytic methane conversion, although it is not uncommon in thermocatalysis to evaluate a catalyst with such a long reaction time[6,32]. TOF and TON, reflecting the efficiency and stability of a catalyst, were used to assess the PdCu nanoalloy co-catalyst against other photocatalysts, as shown in Fig. 1e (the detailed calculation process of TOF and TON was shown in Methods). The reported representative photocatalysts in methane conversion to C_2 products generally exhibit a very small TON of <10 and a moderate TOF of <5 h^{-1}, and two very recent benchmark work achieved TON of 442 h [14]and TOF of 25 h^{-1} [23], respectively. PdCu/TiO_2 shows the highest turnover frequency (TOF_{PdCu}) of C_2 generation (116 h^{-1}) among all the reported photocatalysts operated at λ > 300 nm and room temperature, being a

https://doi.org/10.1038/s41467-023-41996-y

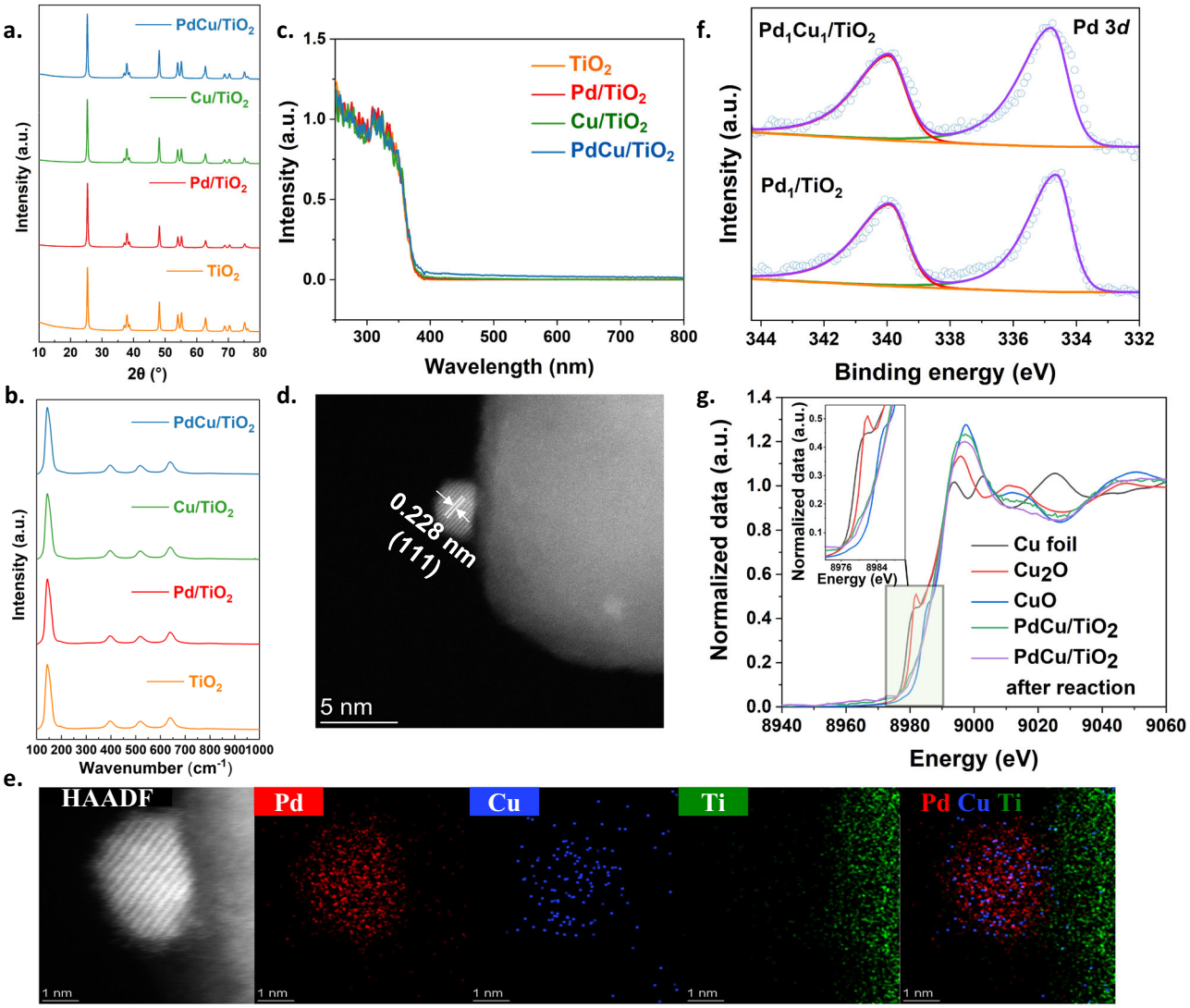

Fig. 2 | Characterisation of the photocatalysts. a XRD spectra of TiO_2, Pd/TiO_2, Cu/TiO_2 and $PdCu/TiO_2$. **b** Raman spectra of TiO_2, Pd/TiO_2, Cu/TiO_2 and $PdCu/TiO_2$. **c** UV-Vis absorption spectra of TiO_2, Pd/TiO_2, Cu/TiO_2 and $PdCu/TiO_2$. **d** HR-TEM image of $PdCu/TiO_2$. **e** HAADF-STEM image and EDX elements mapping of $PdCu/TiO_2$. **f** XPS spectra of Pd_1/TiO_2 and Pd_1Cu_1/TiO_2 (Pd 3*d*) before reaction. **g** Cu K-edge XANES spectra of $PdCu/TiO_2$ and $PdCu/TiO_2$ after reaction in reference to Cu foil, Cu_2O and CuO. Source data are provided as a Source Data file.

new benchmark to the best of our knowledge. Equally importantly, the TON_{PdCu} under the optimised condition is as high as 12,642. This result indicates that PdCu nanoalloy is a stable and effective active site for the selective conversion of methane to C_2 products.

Photocatalysts characterisation

The structure of the photocatalysts was first investigated by powder X-ray diffraction (PXRD), as shown in Fig. 2a. All samples exhibit the typical peaks assigned to the anatase phase (JCPDS no. 84-1286). Neither Pd nor Cu diffraction peaks are observed in all modified samples, probably owing to the low content (Supplementary Table 2) or high dispersion[33]. Raman spectra were further used to investigate the structure (Fig. 2b). Consistent with the results of PXRD, all samples display typical Raman peaks of the anatase phase, at 144 cm^{-1}(E_g), 198 cm^{-1}(E_g), 399 cm^{-1}(B_{1g}), 512 cm^{-1}(A_{1g}), and 639 cm^{-1}(E_g), respectively, suggesting the stable framework of anatase TiO_2 after cocatalyst loading. The ultraviolet-visible diffuse reflectance spectroscopy (UV-Vis DRS) was used to study the photon-absorption properties (Fig. 2c). The absorption (both absorption peak and absorption edge) of all samples remains almost the same, indicating that TiO_2 harvests light for photon-induced carrier generation. A slightly enhanced light absorption at the visible light region after the introduction of co-catalyst nanoparticles is observed, probably due to the interband absorption and/or scattering by these particles[34].

All technologies mentioned above could not provide effective information on the small PdCu nanoalloy particles, thus high-angle annular dark-field scanning transmission electron microscopy (HAADF-STEM) was carried out to gain a microscale view of the $PdCu/TiO_2$ sample (Supplementary Fig. 9). It should be noted that bright nanoparticles are distributed evenly on the supports, with an average size of 2.3 nm. These nanoparticles were further identified by the high-resolution TEM (HR-TEM) image (Fig. 2d), in which the distinct lattice fringes are seen with a d-spacing of 0.228 nm, corresponding to the (111) plane of PdCu nanoalloy[35,36]. To confirm the formation of PdCu nanoalloy, the Energy Dispersive X-Ray Analysis (EDX) was applied to scan the nanoparticles (Fig. 2e, Supplementary Fig. 10). Both Pd and Cu are distributed homogenously within the 2 nm nanoparticle, and a distinct boundary could be identified to distinguish the nanoparticle from TiO_2. Moreover, the element intensity for Pd or Cu can only be visible within the nanoparticle and no signal of individual Pd or Cu can be detected on the TiO_2 support by the STEM image (Supplementary

Fig. 10), confirming the accuracy of the element mapping for PdCu detection. The PdCu nanoalloy structure and the average size remain unchanged after 8 h of reaction (Supplementary Fig. 11–12), indicating the high stability of these nanoparticles.

X-ray photoelectron spectroscopy (XPS) was then carried out to analyse the chemical states of the co-catalyst. Pd_1/TiO_2 and Pd_1Cu_1/TiO_2 with larger loading amounts (1 wt%) of co-catalysts were used in order to have a higher resolution of the spectra. Both samples exhibit similar C_2 yield trend with increasing time, like their counterparts with low loading amount (Supplementary Fig. 13). The Pd 3*d* XPS spectra of Pd_1Cu_1/TiO_2 exhibited two peaks at 334.7 eV Pd $3d_{5/2}$ and 340.0 eV Pd $3d_{3/2}$, respectively (Fig. 2f), and Pd_1/TiO_2 showed similar peaks at 334.6 eV Pd $3d_{5/2}$ and 339.9 eV Pd $3d_{3/2}$, respectively. Both of them were identical to the metallic states of Pd, and the small positive shift of 0.1 eV after the introduction of Cu can be attributed to the interaction between Pd and Cu[37]. No change of Pd 3*d* spectra after 6-hour photocatalytic OCM reaction can be observed, suggesting the high stability of Pd species (Supplementary Fig. 14).

Since the peak positions for $Cu/Cu^{I}/Cu^{II}$ are too closed and the satellite peak for Cu^{II} may be neglected as the background in our case (Supplementary Fig. 15), the Wagner plot was used to analyse the chemical state of Cu species (detailed discussion along with Supplementary Fig. 16 and Supplementary Table 3), which shows the highly possible existence of Cu(II) species in $PdCu/TiO_2$. To further identify the presence of Cu(0) or Cu(I) species, the XAS was carried out. At the Cu K-edge (Fig. 2g), the positive shift in the absorption edge suggests the partial oxidation of Cu species in the PdCu nanoalloy[38]. One can see that the feature of $PdCu/TiO_2$ exhibits a great difference from that of Cu_2O, indicating that CuO is the main oxidised species in the sample. The degree of Cu oxidation relies on the exposure time in air and a longer time may lead to more surface Cu oxidation. This is common in PdCu nanoalloy particles according to previous reports, since the Cu on the surface of PdCu nanoalloy can be oxidised more easily[39,40]. To gain a deeper understanding of the local structure of the alloy nanoparticle, the Fourier transformation magnitudes of k^3–weighted EXAFS data and theoretical fitting for Cu K-edge of $PdCu/TiO_2$ are shown in Supplementary Fig. 17. The spectrum shows two distinguished peaks corresponding to the Cu-O and Cu-Pd. To confirm the characteristics of Cu-Pd rather than Cu-Cu, the EXAFS of Cu K-edge for Cu foil was also fitted (Supplementary Fig. 18). The fitting parameters, e.g., R-bond length, CN-coordination numbers are listed in Supplementary Table 4. The bond length of Cu-Pd is determined to be 2.76 Å with a coordination number of 1.5, larger than that of Cu-Cu bond (2.54 Å) in Cu foil. Such difference is similar to previous reports[39,40], which proves the successful formation of PdCu alloy. After the reaction, $PdCu/TiO_2$ exhibits a slightly positive shift compared with pristine $PdCu/TiO_2$ (Fig. 2g), suggesting a higher oxidation degree[38]. The EXAFS spectrum was further fitted to provide more information (Supplementary Fig. 19 and Supplementary Table 4). Similar to the original $PdCu/TiO_2$, $PdCu/TiO_2$ after the photocatalytic reaction shows distinguished peaks corresponding to the Cu-O and Cu-Pd. However, the coordination number of Cu-O increases after the reaction, corresponding to further oxidation during the reaction system. It is reasonable to see a higher oxidation degree in our system since PdCu is proved as a photohole acceptor later, which can be oxidised readily.

Charge transfer pathway

The charge transfer process of $PdCu/TiO_2$ was investigated via in-situ techniques (EPR, XPS, and NEXAFS). Under dark conditions (Supplementary Fig. 20), the EPR spectrum of pristine TiO_2 itself exhibits some signals related to the small amount of surface oxygen species (e.g., adsorbed superoxide)[41]. Compared with this, two sets of new paramagnetic species appear under light irradiation (Fig. 3a and Supplementary Fig. 20). One set of g values (2.003, 2.014, 2.017) can be attributed to the bridge oxygen radical (e.g., $Ti^{4+}–O^{-}–Ti^{4}$) and another set of g values (2.003, 2.017, 2.027) is owing to the terminal oxygen radical (e.g., $Ti^{4+}–O^{2-}–Ti^{4+}–O^{-}$), which is equivalent to photoholes located on O^{2-} anions[42–44]. After loading of Pd nanoparticles, the intensity of both sets shows an obvious decrease (Fig. 3a), indicating the transfer of photoholes from TiO_2 to Pd nanoparticles or the photoholes in TiO_2 being consumed by the electrons from the d-band of Pd. Moreover, when the argon atmosphere was replaced by a methane atmosphere in the in-situ EPR measurement, the intensity of these two sets of g values was reduced further. Since methane can work as a photohole scavenger to consume photoholes, this result implies that the Pd shows a similar function to methane, which is the photohole acceptor.

The valence-band XPS was used to identify the valence band maximum (VBM) of TiO_2 before and after loading the nanoalloy cocatalyst. Supplementary Fig. 21 shows that some metal-induced occupied states (metallic d-orbital structure) are formed on the VBM of TiO_2 after the introduction of Pd or PdCu nanoalloy, which may provide additional active sites in photocatalysis as reported previously[45]. These states can trap the photoholes from the valence band of TiO_2. It was not able to compare the $PdCu/TiO_2$ here with other samples, due to the inference from the very strong Cu EPR signal (Supplementary Fig. 22)[46].

In-situ XPS was carried out to further confirm the charge transfer from TiO_2 to PdCu (Fig. 3b–d). A positive shift of ~0.3 eV for the Pd $3d_{5/2}$ peak is clearly observed during light irradiation (Fig. 3b), showing direct evidence that Pd works as a hole acceptor during the photocatalytic reaction. However, the signal for Cu 2*p* can not be identified due to the low weight content. Thus, the sample with a higher Pd/Cu precursor mole ratio (1:9) was used for analysis, since this sample exhibits a similar activity trend as $PdCu/TiO_2$ prepared with a Pd/Cu mole ratio of 1:1 (Supplementary Fig. 3). As shown in Fig. 3c, a positive shift of ~0.3 eV can also be observed for Cu $2p_{3/2}$ peak under light irradiation, suggesting that Cu also works as a hole acceptor during the photocatalytic reaction. In contrast to Cu and Pd, Ti $2p_{3/2}$ peak exhibits a negative shift of 0.2 eV under light irradiation (Fig. 3d). This further supports that photoholes are transferred to PdCu and photoelectrons are left on TiO_2.

To further verify the role of the Cu species, the in-situ near-edge X-ray absorption fine structure (NEXAFS) spectra were carried out, as shown in Fig. 3e, f. The NEXAFS spectra are sensitive to reflect the density of states of the orbitals and the Ti, Cu L-edge NEXAFS spectra of $PdCu/TiO_2$ under dark and light illumination were measured. The Ti L-edge and Cu L-edge NEXAFS arise from the 2*p*–3*d* electron transition. Under light illumination, the electrons will be excited from the valence band to the conduction band in TiO_2. The conduction band consists of Ti 3*d* orbital, thus the Ti L-edge NEXAFS feature weakens due to the decreasing density of unoccupied Ti 3*d* states after receiving the electrons from the valence band (Fig. 3e)[47]. In contrast, the intensity of Cu L-edge NEXAFS spectra enhances under light irradiation, suggesting an increasing density of unoccupied Cu 3*d* states[48]. In other words, the photoholes can be transferred from the valence band of TiO_2 to Cu in PdCu, resulting in the increasing density of unoccupied Cu 3*d* states.

The DFT simulations were carried out to provide theoretical support for this role assignment (detailed discussion is shown along with Supplementary Fig. 23 and Supplementary Table 5).

Based on the above discussion, it is reasonable to propose the PdCu nanoalloy as the photohole acceptor. This seems to be beyond the conventional concept in photocatalysis that the metallic nanoparticle on a semiconductor works as an electron acceptor at first glance. However, it should be noted that the conventional concept was proposed based on the work function for the bulk metals. The real work function for small nanoparticles is hard to determine so far due to the limited resolution (~μm) of the probe/beam[49,50]. As the size of PdCu in our photocatalyst is ~2.3 nm, which is far from this range, the

https://doi.org/10.1038/s41467-023-41996-y

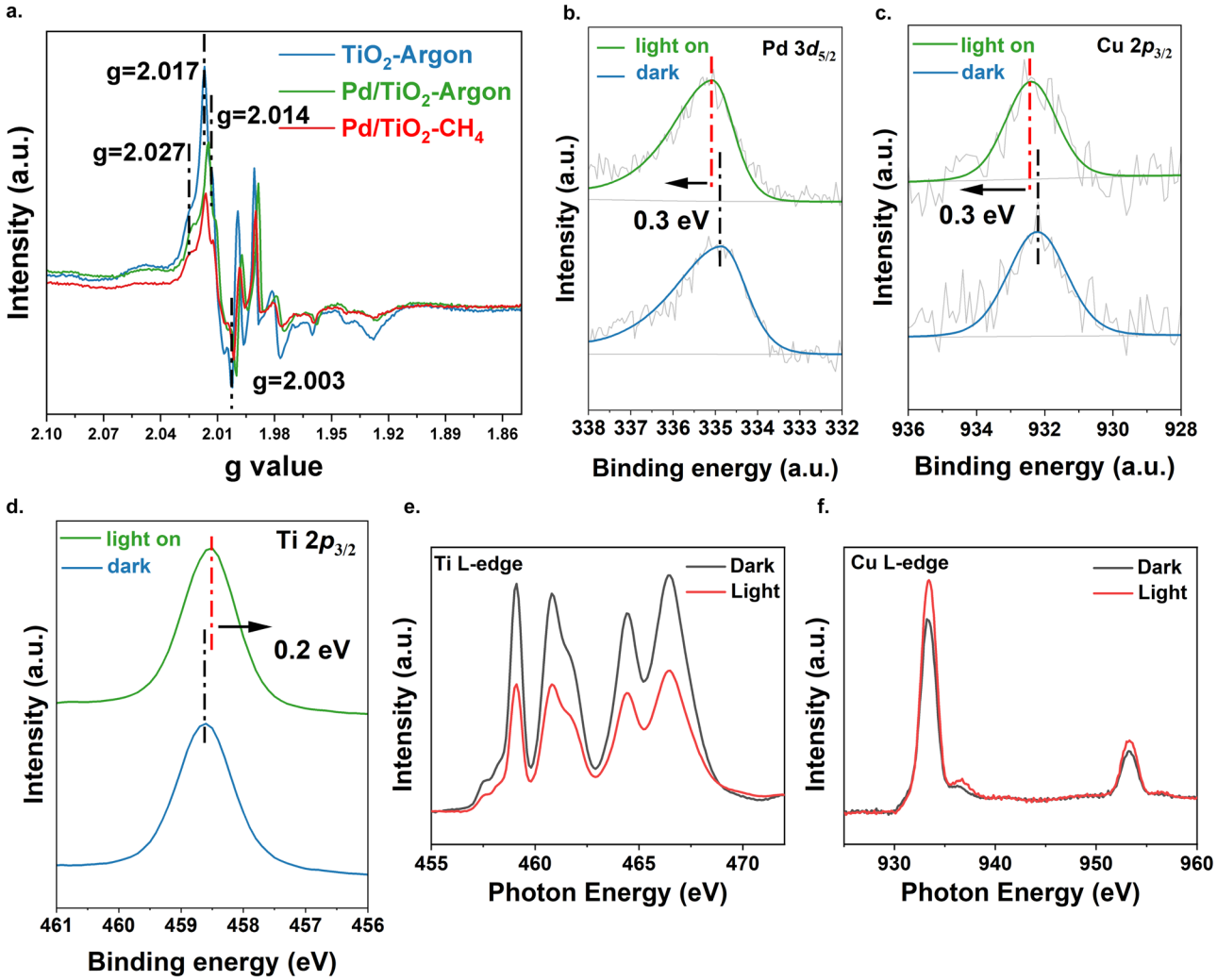

Fig. 3 | Investigation of photon-induced charge transfer. a In-situ EPR spectra of TiO_2 and Pd/TiO_2 in argon atmosphere and CH_4 atmosphere upon light irradiation. **b** In-situ Pd $3d_{5/2}$ XPS spectra of PdCu/TiO_2 under the dark condition and under light irradiation. **c** In-situ Cu $2p_{3/2}$ XPS spectra of PdCu/TiO_2-(1:9) under the dark condition and light irradiation condition. **d** In-situ Ti $2p_{3/2}$ XPS spectra of PdCu/TiO_2-(1:9) under the dark condition and light irradiation condition. **e** Ti L-edge NEXAFS spectra of PdCu/TiO_2 under dark condition and light irradiation. **f** Cu L-edge NEXAFS spectra of PdCu/TiO_2 under dark condition and light irradiation. Source data are provided as a Source Data file.

direct application of the band-alignment theory using the value of bulk metal might be inappropriate. The band-alignment between nanoparticles and semiconductors can be affected by the preparation methods (e.g., photodeposition, wet impregnation, precipitation and colloidal synthesis) and the Schottky barrier is not always present[51]. Thus, different roles (hole/electron acceptor) of same metallic nanoparticle prepared by different techniques are often observed. An advanced four-dimensional STEM technique was developed recently to visualise the charge distribution in metallic Au nanoparticles on $SrTiO_3$, indicating that even the post-synthesis treatments of the same nanoparticle could vary the charge transfer behaviour (positive charges accumulation or negative charges accumulation) during the reaction[52]. Moreover, the accumulation of charges (photoelectrons/photoholes) on the metallic nanoparticle was found to change according to its specific local environment via the direct observation of Kelvin probe force microscopy under illumination[50]. These recent results indicate that particular attention should be paid when proposing the charge transfer pathway[51]. Actually, metal species as hole acceptors have also been proved recently via in-situ XPS, FT-IR, and operando DRIFT, e.g., Pd/TiO_2 in nonoxidative coupling of methane[53], Pt/Ga_2O_3 and Pd/Ga_2O_3 in photocatalytic oxidation of methane with water[54].

The enhanced charge separation was further proved by photoluminescence (PL) and transient photocurrent response (Supplementary Figs. 24 and 25 with discussion alongside). As the photocatalytic OCM reaction involves two redox reactions (methane oxidation by photoholes and oxygen reduction by photoelectrons), the electrochemical oxygen reduction experiments were carried out (Supplementary Fig. 26). All samples present a similar onset potential, because the co-catalysts work as the hole acceptors in all cases and the active sites for oxygen reduction should be located on TiO_2 itself. The enhanced reduction current density after loading of co-catalysts can be attributed to the efficient charge transfer.

The isotope labelling experiment using $^{18}O_2$ as feedstock gas was carried out to double-confirm this half-reaction. As shown in Supplementary Fig. 27a, b, the $H_2{}^{16}O$ peak (m/z = 18) intensity shows a much higher intensity compared with that in the background mass spectra. This result suggests the formation of water during the OCM experiment. To distinguish the oxygen source from TiO_2 or O_2, the isotope labeling experiment using $^{18}O_2$ as the feedstock gas was carried out (Supplementary Fig. 27c). Expectedly, the m/z of 18 assigned to $H_2{}^{16}O$ shows similar intensity in both background mass spectra and the mass spectra using $^{18}O_2$ as the feedstock. Furthermore, the new signal (m/

https://doi.org/10.1038/s41467-023-41996-y

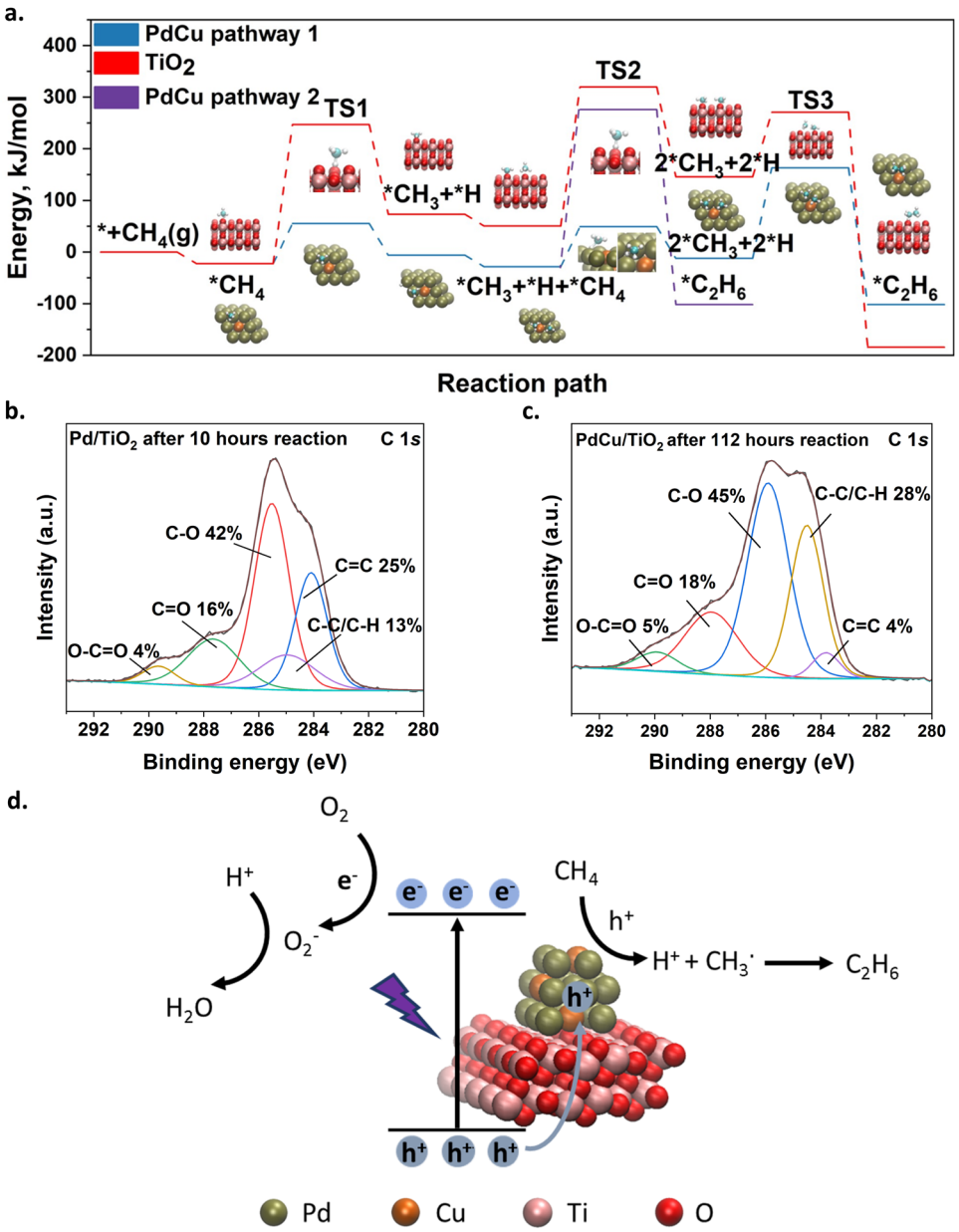

Fig. 4 | Investigation of photocatalytic mechanism. a Calculated energy diagrams for methane conversion to ethane on PdCu and TiO_2. Apart from the methyl radicals coupling pathway (blue line and red line, pathway 1), another pathway (pathway 2, purple line) via the coupling of methyl radicals and methane molecule to form ethane on PdCu is also presented. The ball models for the main pathway on both PdCu and TiO_2 are shown (red – O, pink – Ti, tan – Pd, orange – Cu, teal – C, white – H) **b** XPS spectra (C 1*s*) of Pd/TiO_2 after 10-hour reaction. **c** XPS spectra (C 1*s*) of $PdCu/TiO_2$ after 112-hour reaction. **d** Scheme of photocatalytic OCM over $PdCu/TiO_2$. Source data are provided as a Source Data file.

z = 20) corresponding to $H_2{}^{18}O$ appears using $^{18}O_2$ as the feedstock, indicating the formation of water from the O_2 reduction during the reaction.

Reaction mechanism

After the investigation of the charge transfer, DFT calculations were carried out to investigate the interface reactions. Methane molecules show a final adsorption structure with three C-H bonds pointing down to the surface and one C-H bond pointing up (Supplementary Fig. 28). The length of the C-H bond in the highly symmetric methane molecule in the gas phase was calculated as 1.099 Å and there is almost no change of the C-H distance after adsorption on TiO_2 (Supplementary Table 6). In contrast, the length of C-H (pointing down) could be up to 1.102–1.106 Å when methane was on the surface of Pd or PdCu, indicating a stronger interaction between H of methane and Pd or PdCu than that between H of methane and TiO_2. Such softened C-H bonds in methane through the interaction with the Pd surface have also been observed previously[25], and they were easier to be activated, in particular beneficial for the holes with a lower oxidative potential in Pd.

Then, the reaction barriers for the methane conversion to ethane were determined (Fig. 4a, Supplementary Table 7, 8). The C-H bond in methane requires a large energy (~470 kJ/mol) to cleave it in the gas phase, consistent with previous reports[3]. In contrast, the dissociation of C-H on Pd or PdCu near Pd site has the lowest reaction barrier (TS1) (about 77 kJ/mol), which is more than three times lower than that on TiO_2 (Supplementary Table 7). Thus, the traditional high reaction barrier of the rate-determining step, C-H activation, can be greatly relieved after the introduction of PdCu. After the cleavage of the C-H bond, the following step can be the abstraction of H of another adsorbed methane molecule (pathway 1) or the direct coupling of the

methyl radicals with another adsorbed methane molecule (pathway 2). These two pathways were investigated on different surfaces (Supplementary Table 8). The coupling of two methyl radicals shows the lowest reaction barrier on all surfaces compared with the other two pathways (direct coupling of two methane molecules or coupling one methane with one methyl radical). This pathway is also widely accepted in photocatalytic methane conversion to ethane[2]. In particular, the activation barrier for TS2 of pathway 2 is 130 kJ/mol larger than that of pathway 1 on PdCu, as shown in Fig. 4a. Therefore, the formation of ethane is supposed to follow the coupling of two methyl radicals formed from two separately adsorbed methane molecules. The activation barrier for methyl radicals coupling (TS3) on three catalysts is similar (Supplementary Table 8). This barrier is much less than the C-H activation barrier on TiO_2 (269.5 kJ/mol), indicating that the methane conversion to ethane process on TiO_2 is greatly limited by the rate-determining step of C-H activation and bond dissociation of two separate methane molecules. Therefore, the introduction of Pd can promote the activation of CH_4 and this effect can be maintained after the formation of PdCu nanoalloy.

However, the strong interaction between the reactant and the active sites may also result in the stronger binding of as-formed products (e.g., C_2H_6 in this work), mitigating their desorption and accelerating coking that would block the active sites to cause the catalyst deactivation. This is likely to explain the declining activity trend of Pd/TiO_2 (Supplementary Fig. 5). To examine this assumption, the Raman spectroscopy using a higher energy laser (enhanced by a factor of ten) was carried out to detect coke species in the range of 1000–3000 cm^{-1} (Supplementary Fig. 29). Before the reaction, the Pd/TiO_2 exhibits two peaks with low intensity at around 1350 (D mode) and 1600 cm^{-1} (G mode) and a very small peak at ~2900 cm^{-1} related to the combination of two modes under very strong laser excitation, respectively, which could be attributed to the tiny residue of amorphous carbon adsorbed on the TiO_2 photocatalyst[55–58]. After only 5 h of reaction over Pd/TiO_2, all peak intensities are strongly enhanced. These typical bands confirm the formation of cokes during photocatalytic OCM reaction over Pd/TiO_2, resulting in rapid deactivation. In contrast, such enhancement of peak intensities cannot be observed over the optimised catalyst $PdCu/TiO_2$ even after the 112-hour stability test, suggesting that the introduction of Cu can enhance coke resilience.

The XPS (C 1*s*) has also been conducted to investigate the coke formation of Pd/TiO_2 and $PdCu/TiO_2$ after reactions (Fig. 4b, c). The high-resolution C 1*s* spectra can be deconvoluted into five C species, such as C = C (ca. 284.3 eV), C-H/C-C (ca. 284.8 eV), C-O (ca. 285.6 eV), C = O (ca. 288.0 eV) and O-C = O (ca. 290.0 eV)[59,60], and their proportions are also provided for comparison. Both used catalysts show similar proportions of C-O, C = O, and O-C = O. The C-O can be attributed to the adsorption of some methyl radicals on the surface of TiO_2 and the C = O or O-C = O may be related to the overoxidation of methane to CO_2. Strikingly, these two spent catalysts exhibit differences in the content of C-C/C-H (sp^3) and C = C (sp^2). The ratio between sp^2 C /sp^3 C is ca. 2 and the content of sp^2 C is as high as 25% over Pd/TiO_2 after only 10 hours of reaction, while the ratio decreases to 0.14 with only 4% of sp^2 C can be observed over $PdCu/TiO_2$ even after 112-hour reaction. This indicates that the introduction of Pd can promote dehydrogenation and the C = C species is likely attributed to the formation of cokes. In contrast, Cu may weaken the interaction of the co-catalyst and as-formed products, avoiding the consecutive dehydrogenation to form cokes.

It should be noted that adventitious carbon species can somewhat affect the XPS C 1*s* spectrum[61]. Thus, the TGA-MS was also carried out to have an unambiguous confirmation of coking. The solid coke species on Pd/TiO_2 likely cover the active sites to deactivate Pd/TiO_2 due to the deep dehydrogenation of CH_4 to C species, while the introduction of Cu can avoid the consecutive reaction to form coke (detailed discussion alongside Supplementary Fig. 30). This is consistent with the Raman and XPS results. Similar strategies to use Cu to form an alloy to enhance coke resistance via weaken binding to adsorbates (e.g., ethane in our cases) have been reported in thermocatalysis[17,21,22,62].

DFT calculations were conducted to gain an in-depth understanding of ethane adsorption on Pd and PdCu (the optimised process of different adsorption structures is shown in Supplementary Figs. 31 and 32). As expected, the direct involvement of Cu atoms effectively decreases the adsorption energies of the ethane molecule (Supplementary Table 9), by up to ca. 4 kJ/mol, suggesting the as-formed ethane products can be more easily released from PdCu than from pure Pd, avoiding the consecutive reactions to form cokes. A similar strategy was recently used with the isolation of the Pd site by other components to inhibit coke accumulation in a hydrogenation reaction[37]. Thus, it is reasonable to witness an unchanged activity after even 112 h of reaction over $PdCu/TiO_2$ using the nanoalloy. DFT simulations were also carried out to investigate the catalyst deactivation from the loss of lattice oxygen in TiO_2 and the result suggests that this is not the case in our aerobic reaction system (detailed discussion was shown alongside Supplementary Table 10–12).

A reaction mechanism for photocatalytic OCM reaction over $PdCu/TiO_2$ was proposed as shown in Fig. 4d. Upon light irradiation, photoelectrons excited from the valence band (VB) of TiO_2 to the conduction band (CB) would reduce oxygen to form superoxide radicals on TiO_2, while photoholes from the valence band of TiO_2 would transfer to PdCu nanoalloy where methane is adsorbed. The generated positively charged states would break the pre-softened C-H bonds in the adsorbed methane molecules to form methyl radicals and protons. The coupling of methyl radicals produces ethane molecules and some of them may be further dehydrogenated to form ethylene. The protons would then be consumed by the superoxide radicals to generate water, thus completing the cycle. Moreover, the efficient charge transfer and activation of methane after the introduction of Pd nanoparticles would generate more methyl radicals, which also enhances C_2 selectivity rather than overoxidation to CO_2 owing to the second-order nature of the coupling reaction to form ethane[63]. The formation of nanoalloy with Cu is important to reduce the adsorption energy of the product, thus maintaining a high selectivity to C_2 and avoiding coking. The synergistic effect of PdCu nanoalloy demonstrates a stable, efficient, and selective photocatalytic OCM cycle.

Discussion

In summary, we have reported PdCu nanoalloy (~2.3 nm) decorated TiO_2 as an efficient and stable photocatalyst for OCM in a flow reactor under ambient conditions. The C_2 yield rate of 62 μmol h^{-1} has been achieved with a space velocity of 342,000 mL g_{cat}^{-1} $hour^{-1}$ with a high AQE of ~8.4% at 365 nm thanks to the synergy of Pd and Cu in the nanoalloy. The high stability of the catalyst has also been demonstrated as there is no noticeable decay of the activity during the 112 h test. Thus, both high TON_{PdCu} of 12,642 and TOF_{PdCu} of 116 h^{-1} have been achieved, being a new benchmark in the photocatalytic methane coupling reaction. Fundamentally, the photon-induced holes on TiO_2 can be effectively consumed by the electrons from PdCu nanoalloy, which not only retard the charge recombination but also generate new oxidative orbitals with lower oxidative potential of the reaction sites to drive selective conversion of methane. In particular, Pd works as the active sites to soften and activate C-H bond in methane, while Cu enhances the coke-resilience of the catalysts by decreasing the adsorption energy of as-formed products. This work shows that the assembly of multifunction nanoalloys can be a promising strategy to meet the challenges of efficiency and stability in photocatalytic methane conversion.

Methods

Photocatalysts fabrication

A modified reduction method by $NaBH_4$ was used to prepare noble metals (Pd, Ru, Pt, Ag) decorated TiO_2[64]. In a typical experiment, different amounts of $PdCl_2$ (Aldrich, 99.999%) aqueous solution (2.7 mg_{Pd}/mL) was added to 100 mL of deionised water under stirring. Then, a polymer stabilizer, Poly (vinyl alcohol) (PVA, Aldrich, Mw 9000–10000, 80% hydrolyzed) aqueous solution (1%wt) was added with a weight ratio (polymer/metal) of 0.65. Afterward, certain amount of fresh $NaBH_4$ (Aldrich, ≥96%) aqueous solution (0.1 M) was added with a mole ratio ($NaBH_4$/Pd) of 5 and the solution was stirred for another 30 min. Next, the concentrated H_2SO_4 (0.25 mL) was introduced to the above solution under stirring along with 250 mg of TiO_2 (Millennium PC-50). After stirring for another 1 h, the photocatalyst was obtained by centrifugation, washed with deionsied water for three times, and dried in the oven for 12 h at 60 °C. The photocatalyst synthesized by this method was denoted Pd_x/TiO_2 (x = 0.05, 0.1, 0.5, 1.0, wt%, corresponding to the added amount of Pd weight percentage with respect to TiO_2). The other noble metals decorated TiO_2, denoted M/TiO_2 (M = Pt, Ag, Ru, Au), were synthesized using the similar method with an equal molar amount to Pd in $Pd_{0.1}$/ TiO_2.

For the synthesis of bimetallic alloy decorated TiO_2 photocatalyst, denoted PdM/TiO_2 (M= Cu, Ni, Co, Fe), a modified method was used[65]. Typically, 0.25 mg Pd in the form of $PdCl_2$ aqueous solution (2.7 mg_{Pd}/mL) was added to 45 mL of deionised water, followed by the addition of the equal molar amount of $Cu(NO_3)_2$•$2.5H_2O$ (Alfa Aesar, 98%) aqueous solution. Subsequently, PVA aqueous solution (1%wt) was added with a weight ratio (polymer/Pd) of 1.3, which is two times the amount added in the synthesis of $Pd_{0.1}/TiO_2$. In addition, a certain amount of sodium citrate (Sodium citrate tribasic dihydrate, Sigma-Aldrich, ≥99.0%) aqueous solution (1.4 mg/mL) was mixed at a molar ratio of sodium citrate to metal at 2: 3. Then, the above mixture was purged with argon for more than 20 min under stirring. After the removal of air, a certain amount of fresh $NaBH_4$ aqueous solution (0.1 M) was injected into the above solution with a molar ratio of $NaBH_4$/Pd to10 and the solution was stirred for another 1 h at room temperature with continues argon flow. Afterward, 250 mg of TiO_2 was added to the above solution and the mixture was allowed to stir for another 0.5 h. The photocatalysts were collected by centrifugation, washed three times with deionised water, and dried in a vacuum oven overnight. For the other metals (Ni, Co, Fe), a similar procedure was conducted except for the change of the metal nitrate precursors. For the synthesis of controlling samples Cu/TiO_2, a similar procedure was conducted apart from the introduction of related metal precursors. For the synthesis of the sample (Pd_1Cu_1/TiO_2-large) with a large loading amount (1%wt of Pd and equal molar amount of Cu), a similar procedure was carried out except the ten times higher amount of related chemicals.

Characterisation

The powder X-ray (XRD) spectra were measured with a Rigaku SmartLab SE using a Cu Kα1 source (60 kV, 60 mA). Raman spectroscopy was performed at Renishaw InVia Raman Microscope with a 442 nm laser. Ultraviolet-visible diffuse reflectance spectroscopy (UV-Vis DRS) was recorded by a SHIMADZU UV-2550 in reflectance mode using standard $BaSO_4$ powder as a reference. UV-Probe software was used to convert the reflectance to absorbance via Kubelka-Munk transformation. XPS Analysis was carried out in two instruments. Most samples were measured using Kratos Axis SUPRA XPS while the Cu 2*p* of PdCu/TiO_2-large were measured with a Thermoscientific XPS K-alpha with more scans to obtain high signal-to-noise spectra. In-situ XPS experiment was conducted using a Thermo Fisher ESCALAB 250Xi equipped with a 365 LED light source. All the XPS analysis was performed with CasaXPS software and the spectra were calibrated with C 1 s peak at 284.8 eV. PL spectroscopy was collected by Renishaw InVia Raman with a 325 nm excitation laser. The X-ray absorption spectra (XAS) were collected at the 4B9A beamline in Beijing Synchrotron Radiation Facility (BSRF), China. The storage rings of BSRF were carried out at 2.5 GeV and a stable current of 400 mA. The data collection was conducted in fluorescence mode under ambient conditions using a Si (111) double-crystal monochromator and a Lytle detector. Data analysis and fitting were performed by the Athena and Artemis programs of Demeter software packages using the FEFF6 program[66,67]. A standard Cu foil was used for the energy calibration which was measured as a reference. A linear function was subtracted from the pre-edge region, then the edge jump was normalised using Athena. For EXAFS modelling, the global amplitude EXAFS (e.g., coordination numbers, the distance to the neighboring atom) were analyzed by nonlinear fitting of the Fourier-transformed data in *R*-space using Artemis. The EXAFS of the Cu foil was first fitted and the obtained amplitude reduction factor S_0^2 value was applied to analyse the coordination numbers in the Cu-O/Pd scattering path in $PdCu/TiO_2$. STEM imaging was conducted using a double Cs aberration-corrected FEI Titan[3] Themis 60-300 equipped with an X-FEG gun, a monochromator, and an XEDS ChemiSTEM. The element content was measured by a USA Perkin Elmer 8300 ICP-OES and a Z-2000 HITACHI Atomic Absorption Spectrophotometers (AAS). In-situ EPR was measured using an NRUKER E500-9.5/1.2 spectrometer with a 365 nm LED light source (71 W) under argon, air and CH_4 atmosphere, respectively at 100 K. During the EPR experiments, powder samples (~13 mg) were added in quartz tubes and sealed with septa, then purging by different atmosphere. In-situ Near-edge X-ray absorption fine structure (NEXAFS) spectra were collected at Photoemission End-station (BL10B) in the National Synchrotron Radiation Laboratory (NSRL) in Hefei, China. The data collection was carried out in the total electron yield mode under ambient conditions with a 320 nm LED placed 15 cm in front of the sample. The photon energy was calibrated by the 4*f* spectral peak of a freshly sputtered gold wafer.

(Photo)electrochemical measurements

The electrochemical oxygen reduction reactions were conducted on a Metrohm Autolab potentiostat with a three-electrode system. A photocatalyst-loaded glassy carbon rotating disk (RDE, 3 mm diameter) was used as a working electrode, a glassy carbon rod worked as a counter electrode and Hg/HgO (1 M NaOH) was used as a reference electrode in O_2 saturated 0.1 M of KOH electrolyte, respectively. For the preparation of the working electrode, 4 mg of photocatalysts powder was added into 1 mL of suspension containing 700 µL of deionised water, 264 µL of ethanol, and 36 µL of nafion solution (Sigma-aldrich, Nafion® 117 solution, 5 w/w). After sonication for 30 minutes, a homogenous ink was obtained and 5 µL of the ink was deposited onto the glassy carbon RDE, followed by rotating drying for 1 h under room temperature. Linear sweep voltammograms (LSV) were carried out at a rotation rate of 1600 rpm and a scan rate of 10 mV s^{-1} in the voltage range of 0.2–1.1 V vs. RHE. The photocurrent investigation was carried out on Gamry Instrument Interface 5000E potentiostat under chopped illumination. Typically, 10 µL of the ink prepared using the same recipe as that used in the oxygen reduction reaction was spin-coated on a 0.5 × 1 cm FTO glass with an exposure area of 0.5 × 0.5 cm at 500 rpm for 0.5 min followed by 1000 rpm for 4 min. The process was repeated 3 times. After drying at 80 °C for 120 min, the photocatalyst coated FTO electrode was installed as a working electrode, the Pt plate worked as the counter electrode and Ag/AgCl/3 M KCl was used as the reference electrode in 0.1 M Na_2SO_4 electrolyte. The applied potential was set as 0.2 V vs. Ag/AgCl and a 450 W Xe lamp equipped with an AM 1.5 G filter was used as the light source to maintain the light intensity at 100 mW cm^{-2}. Samples with a geometric area of around 0.25 cm^2 were illuminated from the front side (electrode-electrolyte side). The light illumination was chopped for every 20 s during the whole measuring period.

Photocatalytic reaction for methane conversion

The photocatalytic OCM reaction was conducted in a flow reactor (Supplementary Fig. 33) equipped with a 365 nm LED (Beijing Perfect Light, PLS-LED 100). In a typical experiment, 50 mg of sample was dispersed in 50 mL of deionized water and the mixture was allowed to sonicate for at least 15 min until to achieve a good dispersion. Afterward, the mixture was filtered with a membrane (glass fibre, diameter 37 mm) to obtain a uniform film. After drying the film in the oven, the film was added in the reactor and fixed with a stainless ring, followed by the sealing with a rubber O-ring and a cover. The thermocouple was inserted from the bottom of the reactor and its probe could reach the position of the catalyst bed. Then, the temperature of the system was monitored via the control panel during the reaction. The temperature was 30 °C during the reaction. Three mass flow controllers (MFC, Bronkhorst) were used to control the flow rates of air (BOC, 99.999%), methane (10%, v/v, methane/argon, BOC, 99.999%), and argon (BOC, 99.999%), respectively. To investigate the influences of different ratios of CH_4 to O_2, the real ratio was tuned to 53:1, 114:1, 176:1, and 373:1, respectively after a few calibrations (excluding the influence of temperature and gas line pressure). Before each photocatalytic OCM reaction, the system was purged using the gas mixture at a certain ratio to reach an equilibrium (approximately 90 min). Then, the 365 nm LED (40 W) irradiated from the top quartz window of the reactor and the outlet gases were flowed to two different GCs (Agilent 7820 and Varian 450) to online quantify all the gas products. The permanent gases (e.g., N_2, O_2, H_2, CH_4) were firstly separated from other heavier gas components (e.g., CO_2, C_{2+} products) by a CarbonPlot column, then separated on a Molesieve 5 A column for a final analysis by the thermal conductivity detector (TCD) of Agilent 7820. The organic products, e.g., C_2H_4, C_2H_6, and C_3H_8 was analysed by the flame ionization detector (FID) with an HP-PLOT Q column in the Agilent 7820 machine. The FID in the Varian 450 GC was equipped with a methaniser to quantify the low concentration of CO_2 and CO (*Note*: some work used a TCD detector to analyse CO and CO_2 instead of an FID detector with a mechaniser, the former has a much lower sensitivity than the latter and might lead to an overestimation of the selectivity). For the long-term experiment running, the ratio of CH_4 to O_2 was set as 373: 1, and the experiment was started after reaching equilibrium in each morning and stopped in the evening. (*Note*: Due to the safety requirement, the overnight run was not allowed with such high CH_4/O_2 flow rates. Therefore, the long-time run was carried out by consecutive 20 days run with each day on average 6-hour reaction time).

Calculation of the C_2 selectivity

The selectivity was calculated based on the observable products, including C_2H_6, C_2H_4, C_3H_8, and CO_2. The C_2 selectivity was calculated using the formula below:

$$C_2\ selectivity = \frac{2\times(n_{C2H6}+n_{C2H4})}{2\times n_{C2H6}+2\times n_{C2H4}+3\times n_{C3H8}+n_{CO2}}\times 100\%$$

in which n is the molar rate of different products.

Calculation of apparent quantum efficiency (AQE)

The calculation of apparent quantum efficiency was based on the conversion of methane using the formula shown below:

$$\mathrm{AQE} = \frac{(2\times n_{C2H6}+4\times n_{C2H4}+4\times n_{C3H8}+8\times n_{CO2})\times N_A}{Number\ of\ incdient\ photons}\times 100\%,$$

in which n is the molar generation rate of different products, N_A is the Avogadro constant, and the irradiation area was approximately 7 cm^2. The light intensity was 160 mw/cm^2.

Calculation of Turnover frequency (TOF) and Turnover number (TON)

The calculation of TON was based on the C_2 product yields over the active sites PdCu alloy nanoparticle,

$$\text{Moles of } C_2 \text{ yield} = 5158\ \mu\text{mol}$$

$$\text{Catalyst amount} = 50\ \text{mg}$$

$$\text{PdCu molar amount} = \frac{Catalyst\ amount\times Pd\ concentration}{The\ atomic\ weight\ of\ Pd} + \frac{Catalyst\ amount\times Cu\ concentration}{The\ atomic\ weight\ of\ Cu} = 0.816\mu\text{mol}$$

$$\mathrm{TON} = \frac{Moles\ of\ C_2\ yield\times 2}{PdCu\ molar\ amount} = 12{,}642$$

$$\mathrm{TOF} = \frac{C_2\ yield\ rate\times 2}{PdCu\ molar\ amount} = 116\mathrm{h}^{-1}$$

Noted: For the TON and TOF of other works presented in Fig. 1e, the calculation was based on the active site, such as noble metal co-catalyst in their stability test periods. For those with more than one co-catalyst, the calculation was based on the sum of the co-catalysts amount used for CH_4 activation.

Isotope labelling experiment

For the isotope labelling experiment, a similar photocatalytic process was conducted except $^{13}CH_4$ (^{13}C enrichment >99% atom, Wuhan Newradar Gas Co.) or $^{18}O_2$ (^{18}O enrichment >99% atom, Wuhan Newradar Gas Co.) was used as the feed gas. Typically, 20 mg PdCu/TiO_2 photocatalyst has been used in a flow reactor and a total flow rate of 120 mL/min^{-1} (CH_4: O_2 = 80: 1) was introduced under 300 W Xe lamp irradiation. The products containing C-isotope/O-isotope was analysed by an on-line MS (QIC-20, Heiden Analytical Ltd.).

Computational details

Density-functional theory (DFT) calculations were performed using CRYSTAL17 software[68], with the PBE functional[69] and the D3 dispersion correction[70], with a localised basis set and pseudopotential for Pd[71], and localised all-electron basis sets for Cu[72], Ti, O[73], C and H[74] obtained from the CRYSTAL web site[75]. Pd and PdCu alloy were modeled using 2D-periodic (111)-oriented stabs with three atomic layers and a 3 × 3 extended surface unit cell, using the lattice parameters optimised for bulk Pd, with slabs separated by a 500 Å vacuum gap. In the PdCu alloy, one out of nine Pd atoms in each layer was replaced by a Cu atom. TiO_2 was modelled as a periodic slab of anatase with the (101) surface orientation and a 2 × 2 extended surface unit cell, with the thickness of 8 atomic layers, using the lattice parameters optimised for bulk anatase, with slabs separated by a 500 Å vacuum gap. Single methane or ethane molecules were adsorbed on one side of each slab, in a range of positions. Optimisation calculations of adsorbates on Pd and PdCu were carried out using a 4 × 4 *k*-point grid sampled using the Monkhorst-Pack method, while optimisations on TiO_2 were carried out using a 2 × 2 *k*-point grid. All atom positions were fully optimised. Binding energies were calculated including the basis set superposition error correction[76]. Images of the calculated structures were produced using VMD software[77]. Reaction paths were calculated using the distinguished reaction coordinate method implemented in CRYSTAL17, by defining the reaction coordinate as the C-H distance (for C-H dissociation) or the C-C distance (for methane or methyl reaction to form ethane)[78]. To calculate the densities of electronic states in TiO_2/Pd and TiO_2/PdCu combined systems, we optimised interfaces containing (a)

a finite $Pd_{24}Cu_3$ nanoparticle (ratio Pd:Cu = 8:1) adsorbed on the (2 × 2)-extended TiO_2 anatase (101) slab; (b) a commensurate supercell of (4 × 4)-extended three-layer Pd nanosheet adsorbed on the same (2 × 2)-extended TiO_2 anatase (101) surface. In the latter case, we considered (i) a pure three-layer Pd nanosheet, (ii) the same Pd nanosheet doped with randomly distributed Cu atoms with the ratio Pd:Cu = 9:1, and (iii) the same Pd nanosheet topped with a single layer of Cu. Optimisations were carried out as described above, using the 4 × 4 k-point grid. The density of electronic states of this combined system was then calculated using a 16 × 16 *k*-point grid.

Statistics and reproducibility

No statistical method was used to predetermine sample size and no data were excluded from the analyses

Data availability

All data supporting the findings of this study are available within the paper, supplementary information files and the provided source data files. Source data are provided with this paper.

References

1. Feng, X. et al. Metal-organic framework stabilizes a low-coordinate iridium complex for catalytic methane borylation. *J. Am. Chem. Soc.* **141**, 11196–111203 (2019).
2. Li, X., Wang, C. & Tang, J. Methane transformation by photocatalysis. *Nat. Rev. Mater.* **7**, 617–632 (2022).
3. Schwach, P., Pan, X. & Bao, X. Direct conversion of methane to value-added chemicals over heterogeneous catalysts: challenges and prospects. *Chem. Rev.* **117**, 8497–8520 (2017).
4. Guo, X. et al. Direct, nonoxidative conversion of methane to ethylene, aromatics, and hydrogen. *Science* **344**, 616–619 (2014).
5. Díaz-Urrutia, C. & Ott, T. Activation of methane: a selective industrial route to methanesulfonic acid. *Science* **363**, 1326–1329 (2019).
6. Song, Y. et al. Dry reforming of methane by stable Ni–Mo nanocatalysts on single-crystalline MgO. *Science* **367**, 777–781 (2020).
7. Song, H., Meng, X., Wang, Z., Liu, H. & Ye, J. Solar-energy-mediated methane conversion. *Joule* **3**, 1606–1636 (2019).
8. Meng, X. et al. Direct methane conversion under mild condition by Thermo-, Electro-, or Photocatalysis. *Chem* **5**, 2296–2325 (2019).
9. Takata, T. et al. Photocatalytic water splitting with a quantum efficiency of almost unity. *Nature* **581**, 411–414 (2020).
10. Li, J. et al. Self-adaptive dual-metal-site pairs in metal-organic frameworks for selective CO2 photoreduction to CH4. *Nat. Catal.* **4**, 719–729 (2021).
11. Farrell, B. L., Igenegbai, V. O. & Linic, S. A viewpoint on direct methane conversion to ethane and ethylene using oxidative coupling on solid catalysts. *ACS Catal.* **6**, 4340–4346 (2016).
12. Li, X., Xie, J., Rao, H., Wang, C. & Tang, J. Platinum- and CuOx -decorated TiO2 photocatalyst for oxidative coupling of methane to C2 hydrocarbons in a flow reactor. *Angew. Chem. Int. Ed.* **59**, 19702–19707 (2020).
13. Ishimaru, M., Amano, F., Akamoto, C. & Yamazoe, S. Methane coupling and hydrogen evolution induced by palladium-loaded gallium oxide photocatalysts in the presence of water vapor. *J. Catal.* **397**, 192–200 (2021).
14. Lang, J., Ma, Y., Wu, X., Jiang, Y. & Hu, Y. H. Highly efficient light-driven methane coupling under ambient conditions based on an integrated design of a photocatalytic system. *Green. Chem.* **22**, 4669–4675 (2020).
15. Song, S. et al. A selective Au-ZnO/TiO2 hybrid photocatalyst for oxidative coupling of methane to ethane with dioxygen. *Nat. Catal.* **4**, 1032–1042 (2021).
16. Besenbacher, F. et al. Design of a surface alloy catalyst for steam reforming. *Science* **279**, 1913–1915 (1998).
17. Song, K. et al. Effect of alloy composition on catalytic performance and coke-resistance property of Ni-Cu/Mg(Al)O catalysts for dry reforming of methane. *Appl. Catal. B Environ.* **239**, 324–333 (2018).
18. Kudo, A. & Miseki, Y. Heterogeneous photocatalyst materials for water splitting. *Chem. Soc. Rev.* **38**, 253–278 (2009).
19. Wang, Y., Hu, P., Yang, J., Zhu, Y. & Chen, D. C–H bond activation in light alkanes: a theoretical perspective. *Chem. Soc. Rev.* **50**, 4299–4358 (2021).
20. Singh, S. P., Anzai, A., Kawaharasaki, S., Yamamoto, A. & Yoshida, H. Non-oxidative coupling of methane over Pd-loaded gallium oxide photocatalysts in a flow reactor. *Catal. Today* **375**, 264–272 (2021).
21. Marcinkowski, M. D. et al. Pt/Cu single-atom alloys as coke-resistant catalysts for efficient C-H activation. *Nat. Chem.* **10**, 325–332 (2018).
22. Wolfbeisser, A. et al. Surface composition changes of CuNi-ZrO2 during methane decomposition: an operando NAP-XPS and density functional study. *Catal. Today* **283**, 134–143 (2017).
23. Wu, X. Y. et al. Visible-light driven room-temperature coupling of methane to ethane by atomically dispersed Au on WO3. *J. Energy Chem.* **61**, 195–202 (2021).
24. Lang, S. M., Frank, A. & Bernhardt, T. M. Activation and catalytic dehydrogenation of methane on small Pdx+ and PdxO+ clusters. *J. Phys. Chem. C.* **117**, 9791–9800 (2013).
25. Koitaya, T., Ishikawa, A., Yoshimoto, S. & Yoshinobu, J. C-H Bond Activation of Methane through Electronic Interaction with Pd(110). *J. Phys. Chem. C.* **125**, 1368–1377 (2021).
26. He, J. et al. CdS nanowires decorated with ultrathin MoS2 nanosheets as an efficient photocatalyst for hydrogen evolution. *ChemSusChem* **9**, 624–630 (2016).
27. Xie, J. et al. Highly selective oxidation of methane to methanol at ambient conditions by titanium dioxide-supported iron species. *Nat. Catal.* **1**, 889–896 (2018).
28. Meng, Y. et al. Theoretical research on a coke-resistant catalyst for the partial oxidation of methane: Pt/Cu single-atom alloys. *N. J. Chem.* **44**, 3922–3929 (2020).
29. Chen, X. et al. Photocatalytic oxidation of methane over silver decorated zinc oxide nanocatalysts. *Nat. Commun.* **7**, 12273 (2016).
30. Arndt, S. et al. A critical assessment of Li/MgO-based catalysts for the oxidative coupling of methane. *Catal. Rev.* **53**, 424–514 (2011).
31. Si, J. et al. Oxidative coupling of methane: examining the inactivity of the MnOx -Na2WO4/SiO2 catalyst at low temperature. *Angew. Chem. Int. Ed.* **61**, e202117201 (2022).
32. Tian, J. et al. Direct conversion of methane to formaldehyde and CO on B_2O_3 catalysts. *Nat. Commun.* **11**, 5693 (2020).
33. Yu, X. et al. Stoichiometric methane conversion to ethane using photochemical looping at ambient temperature. *Nat. Energy* **5**, 511–519 (2020).
34. Sorcar, S. et al. CO_2, water, and sunlight to hydrocarbon fuels: a sustained sunlight to fuel (Joule-to-Joule) photoconversion efficiency of 1. *Energy Environ. Sci.* **12**, 2685–2696 (2019).
35. Guo, Z., Kang, X., Zheng, X., Huang, J. & Chen, S. PdCu alloy nanoparticles supported on CeO_2 nanorods: enhanced electrocatalytic activity by synergy of compressive strain, PdO and oxygen vacancy. *J. Catal.* **374**, 101–109 (2019).
36. Wang, F. et al. Monodisperse CuPd alloy nanoparticles supported on reduced graphene oxide as efficient catalyst for directed C–H activation. *Catal. Commun.* **153**, 106296 (2021).
37. Liu, F. et al. Integration of bimetallic electronic synergy with oxide site isolation improves the selective hydrogenation of acetylene. *Angew. Chem. Int. Ed.* **60**, 19324–19330 (2021).
38. Yin, Z. et al. Highly selective palladium-copper bimetallic electrocatalysts for the electrochemical reduction of CO_2 to CO. *Nano Energy* **27**, 35–43 (2016).
39. Jia, X. et al. Low-crystalline PdCu alloy on large-area ultrathin 2D carbon nitride nanosheets for efficient photocatalytic Suzuki coupling. *Appl. Catal. B Environ.* **300**, 120756 (2022).

40. Long, R. et al. Isolation of Cu Atoms in Pd Lattice: forming highly selective sites for photocatalytic conversion of CO_2 to CH_4. *J. Am. Chem. Soc.* **139**, 4486–4492 (2017).
41. Feng, N. et al. Efficient and selective photocatalytic CH_4 conversion to CH_3OH with O_2 by controlling overoxidation on TiO_2. *Nat. Commun.* **12**, 4652 (2021).
42. Hirakawa, T., Nakaoka, Y., Nishino, J. & Nosaka, Y. Primary passages for various TiO_2 photocatalysts studied by means of luminol chemiluminescent probe. *J. Phys. Chem. B* **103**, 4399–4403 (1999).
43. Shoji, S. et al. Photocatalytic uphill conversion of natural gas beyond the limitation of thermal reaction systems. *Nat. Catal.* **3**, 148–153 (2020).
44. Zhu, S. et al. Efficient photooxidation of methane to liquid oxygenates over ZnO nanosheets at atmospheric pressure and near room temperature. *Nano Lett.* **21**, 4122–4128 (2021).
45. Jin, C. et al. Effects of single metal atom (Pt, Pd, Rh and Ru) adsorption on the photocatalytic properties of anatase TiO_2. *Appl. Surf. Sci.* **426**, 639–646 (2017).
46. Li, G., Dimitrijevic, N. M., Chen, L., Rajh, T. & Gray, K. A. Role of surface/interfacial Cu2+ sites in the photocatalytic activity of coupled CuO–TiO_2 nanocomposites. *J. Phys. Chem. C.* **112**, 19040–19044 (2008).
47. Fu, C. et al. Spontaneous bulk-surface charge separation of TiO_2 -{001} nanocrystals leads to high activity in photocatalytic methane combustion. *ACS Catal.* **12**, 6457–6463 (2022).
48. Sun, X. et al. Molecular oxygen enhances H_2O_2 utilization for the photocatalytic conversion of methane to liquid-phase oxygenates. *Nat. Commun.* **13**, 1–12 (2022).
49. Schultz, T. et al. Reliable work function determination of multicomponent surfaces and interfaces: the role of electrostatic potentials in ultraviolet photoelectron spectroscopy. *Adv. Mater. Interfaces* **4**, 1–8 (2017).
50. Liu, Y. et al. Bipolar charge collecting structure enables overall water splitting on ferroelectric photocatalysts. *Nat. Commun.* **13**, 4245 (2022).
51. Farsinezhad, S., Sharma, H. & Shankar, K. Interfacial band alignment for photocatalytic charge separation in TiO_2 nanotube arrays coated with CuPt nanoparticles. *Phys. Chem. Chem. Phys.* **17**, 29723–29733 (2015).
52. Zachman, M. J. et al. Measuring and directing charge transfer in heterogenous catalysts. *Nat. Commun.* **13**, 3253 (2022).
53. Zhang, W. et al. High-performance photocatalytic nonoxidative conversion of methane to ethane and hydrogen by heteroatoms-engineered TiO_2. *Nat. Commun.* **13**, 2806 (2022).
54. Saito, H., Sato, H., Higashi, T. & Sugimoto, T. Beyond reduction cocatalysts: critical role of metal cocatalysts in photocatalytic oxidation of methane with water. *Angew. Chemie Int. Ed.* https://doi.org/10.1002/anie.202306058 (2023).
55. Hardcastle, F. D., Ishihara, H., Sharma, R. & Biris, A. S. Photoelectroactivity and Raman spectroscopy of anodized titania (TiO2) photoactive water-splitting catalysts as a function of oxygen-annealing temperature. *J. Mater. Chem.* **21**, 6337–6345 (2011).
56. Ouyang, Y. & Chen, L. Surface-enhanced Raman scattering studies of few-layer graphene on silver substrate with 514 nm excitation. *J. Mol. Struct.* **992**, 48–51 (2011).
57. Dresselhaus, M. S., Jorio, A., Hofmann, M., Dresselhaus, G. & Saito, R. Perspectives on carbon nanotubes and graphene Raman spectroscopy. *Nano Lett.* **10**, 751–758 (2010).
58. Saito, R., Hofmann, M., Dresselhaus, G., Jorio, A. & Dresselhaus, M. S. Raman spectroscopy of graphene and carbon nanotubes. *Adv. Phys.* **60**, 413–550 (2011).
59. Okpalugo, T. I. T., Papakonstantinou, P., Murphy, H., McLaughlin, J. & Brown, N. M. D. High resolution XPS characterization of chemical functionalised MWCNTs and SWCNTs. *Carbon N. Y.* **43**, 153–161 (2005).
60. Gao, H. et al. Topological defect and sp3/sp2 carbon interface derived from ZIF-8 with linker vacancies for oxygen reduction reaction. *Carbon N. Y.* 131932 https://doi.org/10.1016/j.carbon.2022.10.030 (2022).
61. Greczynski, G. & Hultman, L. X-ray photoelectron spectroscopy: towards reliable binding energy referencing. *Prog. Mater. Sci.* **107**, 100591 (2020).
62. Han, Z. et al. Propane dehydrogenation over Pt-Cu bimetallic catalysts: the nature of coke deposition and the role of copper. *Nanoscale* **6**, 10000–10008 (2014).
63. Su, Y. S., Ying, J. Y. & Green, W. H. Upper bound on the yield for oxidative coupling of methane. *J. Catal.* **218**, 321–333 (2003).
64. Abis, L., Dimitritatos, N., Sankar, M., Freakley, S. J. & Hutchings, G. J. Plasmonic oxidation of glycerol using AuPd/TiO2 catalysts. *Catal. Sci. Technol.* **9**, 5686–5691 (2019).
65. Shu, Y. et al. Hollow echinus-like pdcuco alloy for superior efficient catalysis of ethanol. *ACS Appl. Mater. Interfaces* **10**, 4743–4749 (2018).
66. Zabinsky, S. I., Rehr, J. J., Ankudinov, A., Albers, R. C. & Eller, M. J. Multiple-scattering calculations of x-ray-absorption spectra. *Phys. Rev. B* **52**, 2995–3009 (1995).
67. Ravel, B. & Newville, M. Athena, artemis, hephaestus: data analysis for X-ray absorption spectroscopy using *IFEFFIT*. *J. Synchrotron Radiat.* **12**, 537–541 (2005).
68. Dovesi, R. et al. Quantum-mechanical condensed matter simulations with CRYSTAL. *Wiley Interdiscip. Rev. Comput. Mol. Sci.* **8**, 1–36 (2018).
69. Perdew, J. P., Burke, K. & Ernzerhof, M. Generalized gradient approximation made simple. *Phys. Rev. Lett.* **77**, 3865–3868 (1996).
70. Grimme, S., Antony, J., Ehrlich, S. & Krieg, H. A consistent and accurate ab initio parametrization of density functional dispersion correction (DFT-D) for the 94 elements H-Pu. *J. Chem. Phys.* **132**, 154104 (2010).
71. Pd_HAYWSC-2111d31_kokalj_1998_unpub, https://www.crystal.unito.it/Basis_Sets/palladium.html.
72. Doll, K. & Harrison, N. M. Chlorine adsorption on the Cu(111) surface. *Chem. Phys. Lett.* **317**, 282–289 (2000).
73. Muscat, J. *PhD Thesis*, University of Manchester, UK, 1999
74. Gatti, C., Saunders, V. R. & Roetti, C. Crystal field effects on the topological properties of the electron density in molecular crystals: the case of urea. *J. Chem. Phys.* **101**, 10686–10696 (1994).
75. *CRYSTAL – Basis Sets Library*. https://www.crystal.unito.it/basis-sets.php.
76. Boys, S. F. & Bernardi, F. The calculation of small molecular interactions by the differences of separate total energies. Some procedures with reduced errors. *Mol. Phys.* **19**, 553–566 (1970).
77. *VMD Visual Molecular Dynamics*, https://www.ks.uiuc.edu/Research/vmd/ Humphrey, W., Dalke, A. and Schulten, K., "VMD - Visual Molecular Dynamics", J. Molec. Graphics, 1996, vol. 14, pp. 33–38.
78. Rimola, A. & Zicovich-Wilson, C. M. Localization of Transition States with CRYSTAL09. Zicovich-Wilson. https://tutorials.crystalsolutions.eu/tutorial.html?td=ts&tf=tutorial-ts_crystal
79. Jiang, W. et al. Pd-modified ZnO–Au enabling alkoxy intermediates formation and dehydrogenation for photocatalytic conversion of methane to ethylene. *J. Am. Chem. Soc.* **143**, 269–278 (2021).
80. Meng, L. et al. Gold plasmon-induced photocatalytic dehydrogenative coupling of methane to ethane on polar oxide surfaces. *Energy Environ. Sci.* **11**, 294–298 (2018).
81. Yuliati, L., Hattori, T., Itoh, H. & Yoshida, H. Photocatalytic non-oxidative coupling of methane on gallium oxide and silica-supported gallium oxide. *J. Catal.* **257**, 396–402 (2008).
82. Yuliati, L., Hattori, T. & Yoshida, H. Highly dispersed magnesium oxide species on silica as photoactive sites for photoinduced direct

methane coupling and photoluminescence. *Phys. Chem. Chem. Phys.* **7**, 195 (2005).
83. Yuliati, L., Hamajima, T., Hattori, T. & Yoshida, H. Nonoxidative coupling of methane over supported ceria photocatalysts. *J. Phys. Chem. C.* **112**, 7223–7232 (2008).
84. Wu, S. et al. Ga-doped and Pt-loaded porous TiO_2 –SiO_2 for photocatalytic nonoxidative coupling of methane. *J. Am. Chem. Soc.* **141**, 6592–6600 (2019).
85. Yuliati, L., Itoh, H. & Yoshida, H. Preparation of isolated highly dispersed titanium oxides on silica by sol-gel method for photocatalytic non-oxidative direct methane coupling. *Stud. Surf. Sci. Catal.* **162**, 961–968 (2006).
86. Kato, Y., Matsushita, N., Yoshida, H. & Hattori, T. Highly active silica-alumina-titania catalyst for photoinduced non-oxidative methane coupling. *Catal. Commun.* **3**, 99–103 (2002).
87. Kato, Y., Yoshida, H., Satsuma, A. & Hattori, T. Photoinduced non-oxidative coupling of methane over H-zeolites around room temperature. *Microporous Mesoporous Mater.* **51**, 223–231 (2002).
88. Yuliati, L., Tsubota, M., Satsuma, A., Itoh, H. & Yoshida, H. Photoactive sites on pure silica materials for nonoxidative direct methane coupling. *J. Catal.* **238**, 214–220 (2006).
89. Wang, G. et al. Light-induced nonoxidative coupling of methane using stable solid solutions. *Angew. Chem. - Int. Ed.* **60**, 20760–20764 (2021).
90. Souza, J. D., Souza, V. S. & Scholten, J. D. Synthesis of hybrid zinc-based materials from ionic liquids: a novel route to prepare active Zn catalysts for the photoactivation of water and methane. *ACS Sustain. Chem. Eng.* **7**, 8090–8098 (2019).

Acknowledgements

X.L., C.W., Y.X., and J.T. are thankful for UK EPSRC (EP/S018204/2) and Royal Society Leverhulme Trust Senior Research Fellowship (SRF \R1\21000153). X.L. acknowledges a UCL PhD studentship (GRS and ORS). We are grateful for electrochemistry characterisation by Qian Guo. We are also thankful to Beijing Synchrotron Radiation Facility (BSRF) for XAS data collection and Yue Wen for XRD measurements. We are thankful for Photoemission End-station (BL10B) in the National Synchrotron Radiation Laboratory (NSRL) in Hefei for NEXAFS data collection. Part of X-ray photoelectron (XPS) data collection was performed at the EPSRC National Facility for XPS ("HarwellXPS"), operated by Cardiff University and UCL, under Contract No. PR16195. DFT calculations were performed using the University of Sheffield ShARC cluster, ARCHER2 UK national supercomputer service (http://www.archer2.ac.uk), and Young high-performance cluster at the UK Materials and Molecular Modelling Hub (MMM Hub), which is partially funded by EPSRC (EP/T022213), accessed via N.M.'s membership of the UK's HEC Materials Chemistry Consortium, which is funded by EPSRC (EP/R029431). J.J. Delgado thanks the support by MINECO (Spain), Junta de Andalucia and FEDER through projects PID2020-113809RB-C33 and PY18-2727.

Author contributions

J.T. designed and supervised the progress of the whole project. X.L. proposed the idea, designed and conducted experiments, analysed data and drafted the article. C.W. assisted with the conduction of activity test and characterization. J.Y. Performed the in-situ EPR experiments as well as contributed to the discussion of the EPR results and TPR results. Y.X. contributed to the discussion of the photocatalytic mechanism. Y.Y. and J.Y. carried out in-situ XPS measurements and analysed data. J.J.D. carried out the STEM and analysed data. N.M. conducted the DFT calculations. X.S., X.Z. and W.H. assisted with the isotope-labelling experiment and the NEXAFS measurements. All authors participated the manuscript writing and approved the final version of the manuscript.

Competing interests

The authors declare no competing interests.

Additional information

Supplementary information The online version contains supplementary material available at https://doi.org/10.1038/s41467-023-41996-y.

Correspondence and requests for materials should be addressed to Junwang Tang.

Peer review information *Nature Communications* thanks Marco Altomare and the other, anonymous, reviewer(s) for their contribution to the peer review of this work.